[1] H. Alarcón, O. Ramos, L. Vanel, F. Vittoz, F. Melo and J.-C. Géminard, Phys. Rev. Lett. **105**, 208001 (2010).
[2] J.-C. Géminard, L. Champougny, P. Lidon and F. Melo, Phys. Rev. E **85**, 012301 (2012).
[3] E. Mersch, G. Lumay, F. Boschini and N. Vandewalle, Phys. Rev. E **81**, 041309 (2010).
[4] B. Andreotti, Y. Forterre and O. Pouliquen, *Les milieux granulaires: entre fluide et solide*, (EDP Sciences, CNRS Editions, Paris, 2011).
[5] T. Pahtz, H. J. Herrmann and T. Shinbrot, Nat. Phys. **6**, 364 (2010).
[6] P. W. Dietz and J. R. Melcher, Indust. Eng. Chem. Fund. **17**, 28 (1978).
[7] J.-F. Métayer, P. Richard, A. Faisant and R. Delannay, J. Stat. Mech. P08003 (2010).
[8] J. Israelachvili, *Intermolecular and Surface Forces*, 2 Ed (Academic Press, London, 1992).
[9] A. J. Forsyth, S. R. Hutton, M. J. Rhodes, and C. F. Osborne, Phys. Rev. E **63**, 031302 (2001).
[10] K. Taylor, P. J. King, and M. R. Swift, Phys. Rev. E **78**, 031304 (2008).
[11] N. Olivi-Tran, N. Fraysse, P. Girard, M. Ramonda and D. Chatain, Eur. Phys. J. B **25**, 217 (2002).
[12] H. Gayvallet and J.-C. Géminard, Eur. Phys. J. B **30**, 369 (2002).
[13] L. Bocquet, E. Charlaix, F. Restagno, C. R. Physique **3**, 207 (2002).
[14] T. C. Halsey and A. J. Levine, Phys. Rev. Lett. **80**, 3141 (1998).
[15] N. Mitarai and F. Nori, Adv. Phys. **55**, 1 (2006).
[16] F. Soulié, *Cohésion par capillarité et comportement mécanique de milieux granulaires*, Thèse de Doctorat, Université Montpellier 2 (2005).
[17] M. Scheel , R. Seemann , M. Brinkmann , M. Di Michiel, A. Sheppard , B. Breidenbach and S. Herminghaus, Nature **7**, 189 (2008).
[18] M. Scheel , R. Seemann , M. Brinkmann , M. Di Michiel, A. Sheppard and S. Herminghaus, J. Phys.: Condens. Matter **20**, 494236 (2008).
[19] L. Bocquet, E. Charlaix, S. Ciliberto, J. Crassous, Nature (London) **396**, 735 (1998).
[20] N. Fraysse, H. Thomé and L. Petit, Eur. Phys. J. B **11**, 615 (1999).
[21] J.-C. Géminard and H. Gayvallet, Phys. Rev. E **64**, 041301 (2001).
[22] V. Richefeu, *Approche par éléments discrets 3D du comportement de matériaux granulaires cohésifs faiblement contraints*, Thèse de Doctorat, Université Montpellier 2 (2005).
[23] E. Freyssingeas, M.-J. Dalbe and J.-C. Géminard, Phys. Rev. E **83**, 051307 (2011).
[24] T. H. Kim and C. Hwang, Eng. Geol. **69**, 233 (2003).
[25] T. Gröger, U. Tüzün and D. M. Heyes, Powder Tech. **133**, 203 (2003).
[26] F. Radjai and V. Richefeu, Phil. Trans. R. Soc. A **367**, 5123 (2009).
[27] P. C. F. Møller and D. Bonn, Eur. Phys. Lett. **80**, 38002 (2007).
[28] C. D. Willett, M. J. Adams, S. A. Johnson and J. P. K. Seville, Langmuir **16**, 9396 (2000).
[29] J.-Y. Delenne, M. S. El Youssoufi, F. Cherblanc and J.-C. Bénet, Int. J. Numer. Anal. Meth. Geomech. **28**, 1577 (2004).
[30] H. Alarcón, *Comportamiento mecánico de una capa de material granular sometida a deformaciones en el plano*, PhD Thesis, Universidad de Santiago de Chile, Santiago de Chile (2012).
[31] H. Alarcón, J.-C. Géminard and F. Melo, *to be published in* Phys. Rev. E (2012).
[32] R. M. Nedderman, *Static and Kinematics of Granular Materials*, (Cambridge University Press, Cambridge, England, 1992).

CLAY ALIGNMENT IN ELECTRIC FIELDS

ALINEACIÓN DE ARCILLAS EN CAMPOS ELÉCTRICOS

R. C. Castberg[a †], Z. Rozynek[b], J. O. Fossum[b,d ‡], K. J. Måløy[a,d *], P. Dommersnes[c,d] and E. G. Flekkøy[a,d]

a) Department of Physics, University of Oslo, P.O. Box 1048, NO-0316, Oslo, Norway,
rene@castberg.org†, k.j.maloy@fys.uio.no*
b) Department of Physics, NTNU, Høgskoleringen 5, NO-7491, Trondheim, jon.fossum@ntnu.no‡
c) Matieres et Systemes Complexes, Universite Paris 7, 75253, Paris, France
d) Centre for Advanced Study at the Norwegian Academy of Science and Letters, Drammensveien 78, NO-0271 Oslo, Norway
†, ‡, * corresponding authors

The response of rotational alignment of lithium fluorohectorite (Li-Fh) to an external electric field has been studied by employing image analysis. Large aggregates consisting of many single clay particles were prepared using a sedimentation technique in order to control both their shapes and sizes. Such aggregates have a layered structure which was confirmed by wide-angle X-ray scattering (WAXS) studies. Measuring the electric-field-induced alignment of these particles we obtained a data collapse by plotting $\ln(\theta)$ versus t/E^2, where θ is the rotational angle, t is time and E is the electric field strength.

Se estudia la respuesta de la alineación rotacional de la fluorohectorita de litio (Li-Fh) debido a un campo eléctrico externo mediante análisis de imágenes. Se prepararon grandes agregados consistentes en muchas partículas individuales de arcilla usando una técnica de sedimentación, con el objetivo de controlar tanto sus formas como sus tamaños. Tales agregados poseen una estructura a capas, lo que fue confirmado por dispersión de rayos X de ángulo ancho (WAXS). Midiendo el alineamiento inducido por campo eléctrico de las partículas, obtuvimos un colapso de los datos en un gráfico $\ln(\theta)$ vs. t/E^2 donde θ es el ángulo de rotación, t es el tiempo, y E es la intensidad del campo eléctrico.

PACS: Electrorheological fluids, 47.65.Gx; self-assembly (nanofabrication), 81.16.Dn; X-ray scattering in structure determination, 61.05.cf

INTRODUCTION

On application of an external electric field, clay particles suspended in non-polar and non-conductive carrier fluids (such as silicone oil) will rotate and align themselves [1] such that their stacking direction is normal to the electric field direction. Once these particles have aligned themselves, they will eventually start forming chain-like structures [2, 3, 4]. In order to understand the processes behind chain formation, we have to understand how the individual particles initially orient themselves with the field. From preliminary observations, we find that for small particles this process takes a couple of *ms*, for this reason we prepared larger particles which were easier to manipulate. In this work optical measurements were made of the particles aligning themselves in the electric field and we show that there is a E^2 dependency on the rotation rate.

SAMPLE PREPARATION

Lithium fluorohectorite (Li-Fh) was purchased from Corning Inc., New York in the form of a white powder. Li-Fh is a synthetic 2:1 smectite clay having the nominal chemical formula $Li^{+}_{1.2}[[Mg_{4.8}Li_{1.2}]Si_8O_{20}F_4]^{1.2-}$ per unit cell, where Li is an interlayer exchangeable cation (not to confuse with Li in the crystaline sheet); for more details on structure see reference [5]. Li-Fh has a surface charge of 1.2 e-/unit cell and is a polydisperse clay with platelet diameters ranging from a few hundred *nm* up to several μm [6]. In order to have a better control on the particle shape and size (parameters that may influence the rotation time when particles are subjected to *E*-fields), it was decided to prepare the samples as follows. The Li-Fh powder was mixed with deionized water and stirred for 12 *h* at RT. Next, the solution was transferred to a flat Petri dish and then left for 3 days at RT for water evaporation. During that time the individual clay particles sediment, and generally lie flat on the bottom of the dish and consequently stack on one another as sketched in Figure 2 (a). In order to obtain different particle thicknesses' four different clay concentrations were used, namely 0.5, 1, 2 and 4 *wt.*%. In this proceeding we will present data from the 2 *wt.*%. Once the samples have dried, they were carefully cut into small pieces with desired lengths and widths (see Figure 1).

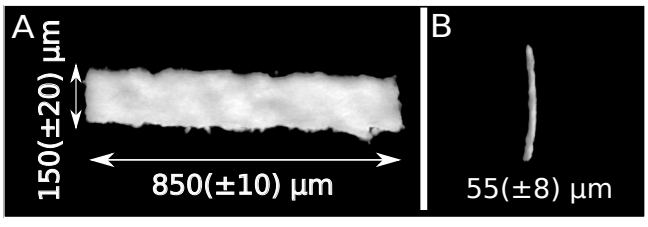

Figure 1: Optical microscopy images of the sample showing length of around 0.85 *mm* (A) and thickness of around 55 μm (B).

SAMPLE CHARACTERISATION

The sample shown in Figure 1, with thickness of around

55 μm, was measured at our home laboratory (NTNU, Norway) using a NanoSTAR X-ray instrument from Bruker AXS, setup in a wide-angle X-ray scattering (WAXS) configuration during the present experiments. This instrument is equipped with a CuKα micro-source emitting X-rays at wavelength of 1.5418 $Å$; and a 2-D detector that collects Bragg diffraction rings. The equipment enabled the investigation of both the orientational distribution of the clay platelet stacks and the characteristic interlamellar distance for monitoring the intercalated water content. The X-ray beam is directed such that it is normal to the sedimentation direction, as shown in Figure 2 (a), i.e. the thickness of the particle. The beam has a diameter of about 0.4 mm and the available scattering q-range for the setup used here was: 0.08 - 1 $Å^{-1}$.

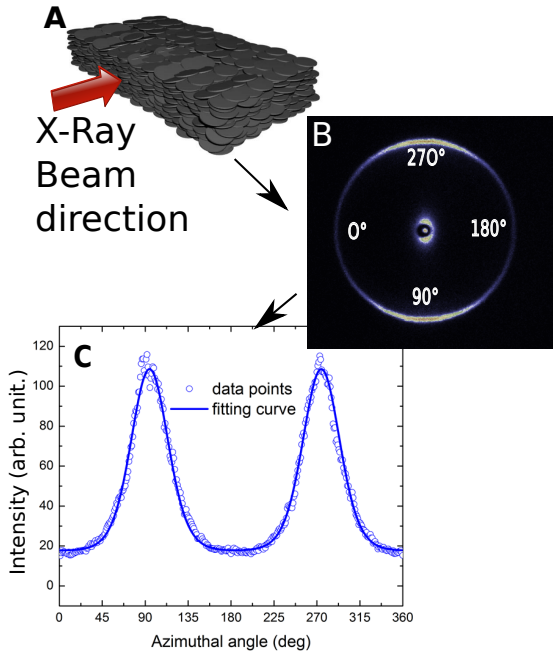

Figure 2: (A) Clay platelets forming an aggregate, (B) resulting in an asymmetry in the WAXS data. (C) The azimuthal plot is made by radial integration of the 2-D WAXS pattern. The parametric fit (solid line) is used to calculated the nematic order parameter (here $S_2 = -0.34 \pm 0.02$).

An example of the two-dimensional WAXS pattern is shown in Figure 2 (b). The 001 Bragg ring that originates from the clay interlamellar distance (between clay crystalline sheets) is anisotropic indicating that the clay particles have a preferential orientation. Since the scattering intensity peaks at 90° and 270° and the direction of the X-ray beam is horizontal, one can conclude that the clay particles are oriented with their stacking direction normal to the X-ray beam, as sketched in Figure 2 (a). When the 2-D WAXS pattern is integrated along the radial direction with a narrow q-range (2θ-angle) around the Bragg ring, one can obtain a 1-D azimuthal plot, as presented in Figure 2(c). This can be fitted to a parametric function (such as Maier-Saupe, see [7, 8]) in order to calculate the nematic order parameter (S_2), which is a qualitative measure of the clay particles' orientation distribution. In this case, the S_2 was found to be -0.34 ± 0.02 (remark: $S_2 = 0$ and $S_2 = -0.5$ indicate no preferential orientation and perfect alignment, respectively).

EXPERIMENTAL SET-UP AND ANALYSIS

The experimental set-up is sketched in Figure 3. Castor oil was used as a hosting liquid to fill the cell. The castor oil has a high viscosity (~ 1000 cSt), ensuring that the particles rotate slowly enough to obtain accurate data. The particle is placed in the centre of the cell such that it is completely surrounded by the castor oil. Initially the particle (prepared as described in the sample preparation section) is aligned with the major axis normal to the electric field, and the narrowest side aligned parallel to the electric field. When the field is then applied the particle starts to rotate such that the major axis is eventually aligned parallel to the field. Each measurement is filmed at 30 fps and then the recording is processed using MATLAB by tracking the particle from frame to frame (using the regionprops function). Its angle is calculated by fitting an ellipse to the particle and measuring the angle of the major axis. For each of the measured field strengths the same particle was used, ensuring that the experiments were as similar as possible.

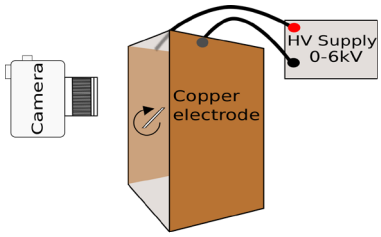

Figure 3: Experimental setup: A video camera is used to film the rotating particle in a glass cell. The two copper electrodes are connected to a high voltage supply capable of supplying up to 5 kV DC. Resulting in an electric field of up to 500 V/mm.

RESULTS AND DISCUSSION

The results for tracking the same particle at different field strengths can be seen in Figure 4. In this plot we see the angle of the particle plotted against the time. It can be clearly seen that the rotation time for the lowest fields (100 V/mm) are considerably longer than for the highest fields (500 V/mm).

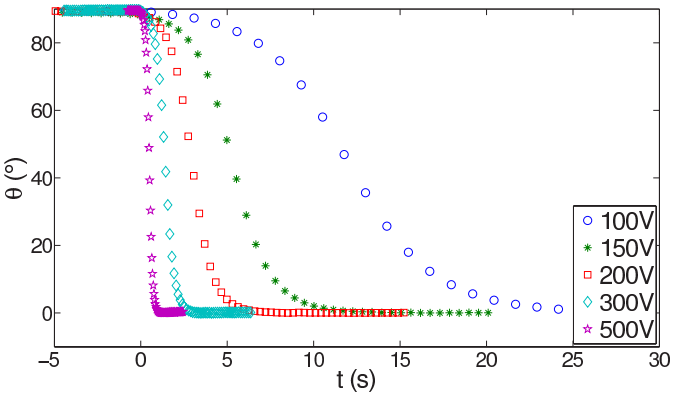

Figure 4: Angle of rotation for a single particle at different electric field strengths. Particle size: $0.85 \times 0.15 \times 0.055$ mm

This is expected as there is an equilibrium between the torque (T) applied from the electric field and the drag of the oil. The torque due to drag in the rotational plane can be written as[9]:

$$T_d = -\zeta_{rot}\dot{\theta}, \tag{1}$$

where ζ_{rot} is the specific rotational drag coefficient in the plane the particle rotates.

The torque due to the electric field is [10,11]

$$\vec{T}_E = (\bar{\chi}\vec{E})\times\vec{E}, \tag{2}$$

which can then be written as

$$T_E = \chi_0 E^2 \sin(\theta)\cos(\theta), \tag{3}$$

where χ_0 is the effective polarizability involving geometric factors. As the data is for the same particle, i.e. the shape and structure are the same, χ_0 is considered a constant.

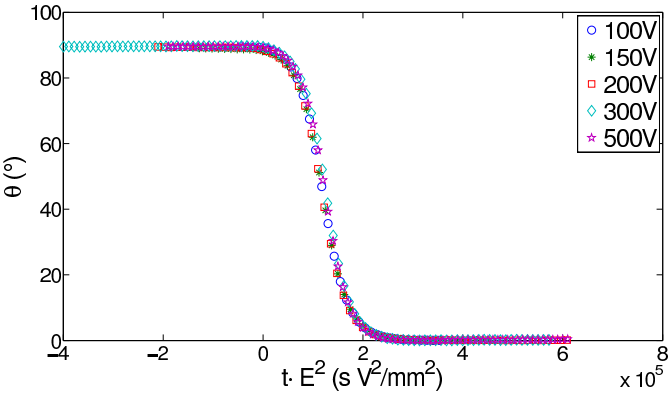

Figure 5: Data collapse of Figure 4, θ plotted against time multiplied by E^2 for different field strengths. Particle size: $0.85 \times 0.15 \times 0.055$ *mm*

We are operating in the low Reynolds number regime ($Re <$ 0.01), and can ignore any inertial effects, hence the electric torque balances the hydrodynamic torque giving

$$\dot{\theta} = -\frac{\chi_0 E^2}{2\zeta_{rot}}\sin(2\theta) = -\frac{1}{2\tau}\sin(2\theta) \tag{4}$$

and thus we obtain

$$\tau \propto \frac{1}{E^2} \tag{5}$$

This is confirmed by way of a data collapse by plotting θ against $t \cdot E^2$, where t is the time and E is the field strength. This can be seen in Figure 5. We should note that we have not treated the anisotropic effects of the dipole that would be encountered as the cylinder rotates. For a more detailed study the reader is referred to Doi and Edwards [9] Solving equation Eq. (4) results in

$$\ln\left(\frac{\tan(\theta)}{\tan(\theta_0)}\right) = -\frac{t-t_0}{\tau}, \tag{6}$$

where t_0 is the time the field is applied, and the corresponding angle $\theta_0 = \theta(t_0)$. We can observe this in Figure 6 where we plot $\ln(\tan(\theta))$ against $t \cdot E^2$ and can see an exponential cut-off, with a slope of -3.4×10^{-5}.

CONCLUSION

From the data we can clearly see that θ scales with time as E^2 as the electric field strength is changed. In future work we wish to determine the effect of the particle geometry, and how multiple water layers affect the rotation time, as in these experiments we only had 1 water layer, and whether the intercalated cations contribute to the dipole moment.

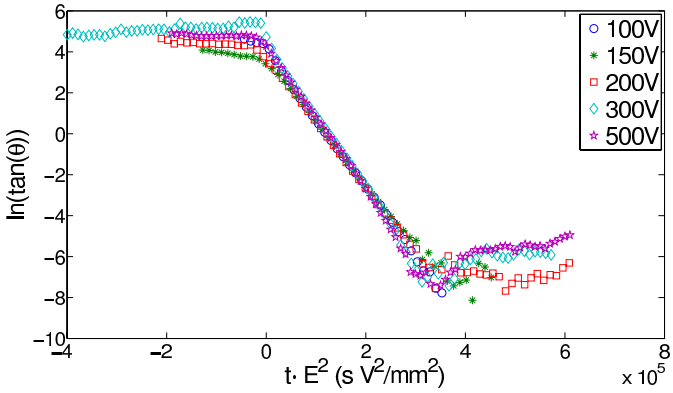

Figure 6: Data collapse of Figure 4, ln (tan (θ)) plotted against time multiplied by E^2 for different field strengths. Particle size: $0.85 \times 0.15 \times 0.055$ *mm*

ACKNOWLEDGEMENTS

This work was supported by the Research Council of Norway through the Nanomat program, project number 182075 and the FRINAT program, project number: 171300.

[1] J. O. Fossum, Y. Méheust, K. P. S. Parmar, K. D. Knudsen, K. J. Måløy and D. M. Fonseca, Europhys. Lett. **74**, 438 (2006).
[2] B. Wang, M. Zhou, Z. Rozynek and J. O. Fossum, J. Mater. Chem. **19**, 1816 (2009).
[3] Z. Rozynek, K. D. Knudsen, J. O. Fossum, Y. Méheust, B. Wang and M. Zhou, J. Phys: Condens. Mat. **22**, 324104 (2008).
[4] Z. Rozynek, H. Mauroy, R. C. Castberg, K. D. Knudsen and J. O. Fossum, Rev. Cub. Fis. **29**, 1E37 (2012).
[5] H. Hemmen, L. R. Alme, J. O. Fossum and Y. Méheust, Phys. Rev. E **82**, 036315 (2010).
[6] P. D. Kaviratna, T. J. Pinnavaia and P. A. Schroeder, J. Phys. Chem. Solids **57**, 1897 (1996).
[7] Y. Méheust, K. D. Knudsen and J. O. Fossum, J. Appl. Cryst. **39**, 661 (2006).
[8] Z. Rozynek, B. Wang, J. O. Fossum and K. D. Knudsen, Eur. Phys. J. E. **35**, 9 (2012).
[9] M. Doi and S. Edwards, *The Theory of Polymer Dynamics*, (Oxford University Press, USA, 1986).
[10] P. Zijlstra, M. van Stee, N. Verhart, Z. Gu and M. Orrit, Phys. Chem. **14**, 4584 (2012).
[11] H-Y Hsu, N. Sharma, R. S. Ruoff and N. A. Patankar, Nanotechnology **16**, 312 (2005).

STRUCTURAL STUDIES OF MIXED NANO-SPHERES AND POLYMERS

ESTUDIOS ESTRUCTURALES EN MEZCLAS DE NANO-ESFERAS Y POLÍMEROS

A. Washington[a], X. Li[a], A. Schofield[c], K. Hong[b], M. R. Fitzsimmons[e] and R. Pynn[a,b,d]

a) Center for the Exploration of Energy and Matter, and Indiana University Department of Physics, Bloomington, Indiana, USA
b) Center for Nanophase Materials Science, Oak Ridge National Laboratory, Oak Ridge, Tennessee 37831, USA
c) School of Physics and Astronomy, University of Edinburgh, Mayfield Road, Edinburgh, Scotland
d) Center for Advanced Studies, Norwegian Academy of Science and Letters, Oslo, Norway
e) Los Alamos National Laboratory, Los Alamos, New Mexico, USA

A newly developed neutron scattering technique known as Spin Echo Small Angle Neutron Scattering (SESANS) allows real-space density correlations to be probed in bulk samples over distances ranging from ~20 *nm* to up to several microns. We have applied this technique to study correlations between polymer-stabilized poly(methyl methacrylate) (PMMA) spheres suspended in either dodecane or decalin. As expected, the data show that for colloid volume factions below about 40%, correlations between PMMA spheres are accurately described by the Percus-Yevick hard-sphere model. When a small amount of polymer is added to the colloidal suspension and when the carrier fluid is a good solvent for the polymer, short-range correlations between PMMA spheres are increased by the presence of the polymer depletant and are in reasonably agreement with calculations using an integral equation model. When higher concentrations of polymers are added, we find that long-range, power-law correlations develop between spheres, even though the sample flows freely. When the solvent is not a good solvent for the polymer depletant, correlations between PMMA spheres are unaffected by the addition of small quantities of polymer.

Una nueva técnica de dispersión de neutrones conocida como espín-eco de dispersión de neutrones de bajo ángulo (SESANS, según sus siglas en inglés) permite medir correlaciones de densidad en el espacio real, para muestras masivas, sobre distancias que van desde unos 20 *nm*, hasta algunas micras. Hemos aplicado esta técnica al estudio de las correlaciones entre esferas poliméricas estabilizadas de polimetil-metacrilato (PMMA) suspendidas en dodecano o decalina. Como se espera, los datos muestran que, para fracciones volumétricas inferiores al ~40%, las correlaciones entre las esferas de PMMA se describen bien por el modelo de Percus-Yevick de esferas-rígidas. Cuando se adiciona una pequeña cantidad de polímero a la suspensión coloidal, y cuando el fluido portador es un buen solvente para el polímero, se incrementan por la presencia del depletante de polímero, y muestran un acuerdo razonable con cálculos según un modelo basado en una ecuación integral. Cuando se usan concentraciones mayores de polímero, encontramos correlaciones de largo alcance entre esferas, del tipo ley de potencia, aún cuando la muestra fluye libremente. Cuando el solvente no disuelve bien el depletante de polímero, las correlaciones entre esferas no se afectan si se agregan pequeñas cantidades de polímero.

PACS: Neutron scattering in structure determination, 61.05.fg; polymer solutions flow properties, 47.57.Ng; structure of polymer solutions , 61.25.he; correlations collective effects, 71.45.Gm

INTRODUCTION

When sterically-stabilized colloidal spheres of poly(methyl methacrylate) (PMMA) are suspended in a hydrocarbon solvent, small angle neutron scattering (SANS) from the mixture can be described using the Percus-Yevick model for hard-sphere correlations [1]. In the present work, our goal was to probe the changes induced in the correlations between the colloidal spheres when an attractive force between them is turned on. To generate this force, we have added small amounts of polymer to generate a depletion interaction between the spheres [7]. Rather than measure the correlations using traditional SANS, we have chosen to use a new technique called spin-echo SANS or SESANS.

SESANS AND SANS

SANS is a widely used method for interrogating the structure of materials on length scales between a few nanometers and roughly 100 *nm*. SANS measurements of a colloidal fluid are described as a product of a form factor –the Fourier transform of the density distribution within each colloidal particle– multiplied by a structure factor which contains information about inter-particle correlations. Unfortunately, much of the latter information is found at large values of the neutron's wavevector transfer, *Q*, where the scattering is strongly damped by the form factor. This makes traditional SANS a good tool for measuring form factors, i.e. the structure of non-interacting monodisperse particles, but a rather poor one for measuring inter-particle correlations in colloids.

SESANS overcomes some of the disadvantages of SANS by Fourier transforming the neutron scattering signal and providing a correlation function in real space [2]. It is

more sensitive to inter-particle correlations than traditional SANS because it exactly Fourier transforms the scattering signal –including the weak signal at large Q which contains information about correlations– before noise is added by the measurement. In addition to this advantage, SESANS measures the same pair correlation function even when a sample scatters strongly whereas SANS patterns obtained with concentrated, strongly scattering dispersions have to be corrected for multiple scattering of neutrons. Finally, the length scale probed by SESANS is larger than for SANS, which makes it a good tool for exploring correlation functions in colloidal fluids containing particles of a few hundred nanometers in diameter.

The correlation function, $G(z)$, measured by SESANS is a projection of the usual Debye density-autocorrelation function on to a particular direction, z. For isotropic fluids such as those studied here the choice of direction onto which the Debye function is projected is irrelevant. Mathematically, $G(z)$ is given by the Abel transform of the Debye correlation function [5].

SESANS works by encoding the scattering angle of each neutron into the Larmor precession phase accumulated as the neutron passes through suitably designed magnetic fields [6]. In a SESANS experiment, the cosine of the total Larmor phase is averaged over the scattered neutron beam and measured as a neutron polarization. Because of the cosine factor, the neutron polarization represents a Fourier transform of the scattered neutron intensity.

We have constructed a SESANS apparatus that can be installed on neutron scattering instruments that provide a polarized neutron beam and the measurements described here have been obtained with this equipment mounted on the Asterix reflectometer at the Los Alamos Neutron Science Center (LANSCE). An account of the SESANS technique, which includes a description of the apparatus used in the measurements described here, is given in reference [6].

RESULTS

The colloidal samples we have used in our experiments were prepared using a published method [3]. The resulting PMMA particles, which had diameters between 200 *nm* and 250 *nm* depending on the sample batch, were suspended in either dodecane or decalin at concentrations between 30% and 50% by volume. In order to adjust the neutron scattering contrast between the PMMA spheres and the carrier fluid, mixtures of deuterated and hydrogenated solvents were used. Decalin is both a reasonable solvent for the polymer depletant used in our experiments (polystyrene) and has an optical refractive index which is close to that of PMMA, ensuring that the van der Waals interactions between the PMMA spheres is minimized. Dodecane, on the other hand, is a relatively poor solvent for polystyrene. For PMMA concentrations up to at least 40% by volume, SESANS shows that the correlations between PMMA particles in freshly sonicated samples are well described by the Percus-Yevick, hard-sphere theory for both dodecane and decalin solvents, as shown in Figures 1 (a) and 1 (b).

When small concentrations of polymer depletant are added, the short-range correlations between particles are increased when they are suspended in decalin. A calculation using integral-equation theory [4] shows that the data in Figure 1 (a) can be described using a short-range, attractive potential that is roughly $2kT$ deep. The magnitude of this potential appears to be approximately the same for polymer molecular weights of 110 *kDa* and 900 *kDa* when the same weight percentage of polymer depletant is used. When the particles are dispersed in dodecane, the addition of polystyrene does not change the inter-particle correlations, at least for polystyrene concentrations up to 1% by weight (cf. Figure 1 (b)). This is probably due to the fact that the PS moelcules tend to collapse in the poor solvent, significantly reducing the depeletion forces.

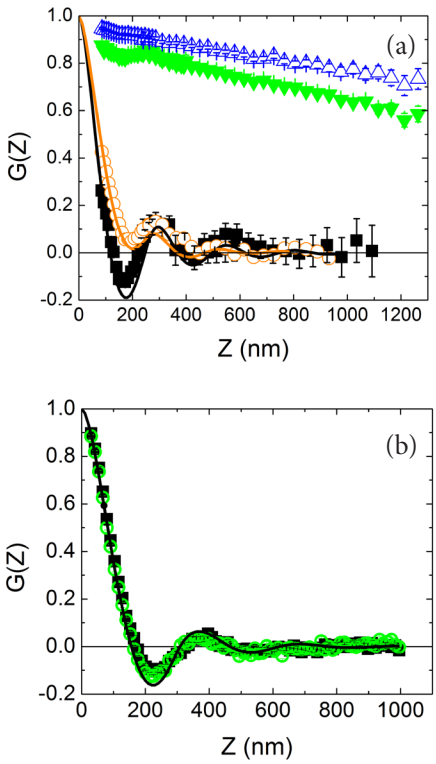

Figure 1: (a) The inter-particle correlation function $G(z)$ for 40% suspensions of 260-*nm*-diameter PMMA spheres in decalin measured by SESANS. Solid squares –PMMA spheres alone; open circles– PMMA with 0.2% 900 *kDa* polystyrene; open triangles PMMA with 1% 900 *kDa* polystyrene; inverted triangles PMMA with 0.5% 900 *kDa* polystyrene. Dark line is Percus-Yevick calculation and the lighter line is result of integral equation calculation with "sticky" spheres. (b) $G(z)$ for a 40% suspension of PMMA spheres in dodecane (solid squares) and with 1% 110 *kDa* polystyrene (open circles). The line is calculated from the Percus-Yevick theory.

For larger concentrations of depletant in the decalin system (greater than roughly 0.3% by weight for polymers with molecular weights of either 110 *kDa* or 900 *kDa*), SESANS indicates that correlations extend out to distances of many particle diameters and that the correlation function $G(z)$ is roughly a linear function over much of the range of inter-particle distances probed (cf. Figure 1 (a)). The correlations

eventually disappear at sufficiently large values of z, indicating the maximum size of the aggregates that have been formed. The linear behavior of $G(z)$ is consistent with a power-law behavior of the Debye correlation function. Although the maximum aggregate size often increases with time over periods of several hours, aggregates can be broken up easily by stirring and sonication. The short-range correlations in aggregates appear to be independent of aggregate size but are slightly different from those obtained with weak sticky potentials that do not result in aggregates. This presumably results from jamming of particles once aggregates are formed.

ACKNOWLEDGEMENTS

This work was funded by the U.S. Department of Energy through its Office of Basic Energy Sciences, Division of Material Science and Engineering (Grant No. DE-FG02-09ER46279). The Los Alamos Neutron Science Center is funded by the U.S. Department of Energy's Office of Basic Energy Sciences under contract DE-AC52-06NA25396 with Los Alamos National Security LLC. Some of the sample preparation was done at the Center for Nanophase Materals Science at Oak Ridge National Laboratory, which is sponsored by the Office of Basic Energy Sciences, U.S. Department of Energy.

[1] A. Moussaid, W. C. K. Poon, P. N. Pusey and M. F. Soliva, Phys. Rev. Lett. **82**, 225 (1999).
[2] R. Pynn, M. R. Fitzsimmons, H. Fritzsche, M. Gierlings, J. Major and A. Jason, Rev. Sci. Instrum. **76**, 053902 (2005).
[3] L Antl, J. W. Goodwin, R. D. Hill, R. H. Ottewill, S. M. Owens, S. Papworth, and J. A. Waters, Colloids And Surfaces **17**, 67 (1986).
[4] X. Li, C. -Y. Shew, Y. Liu, R. Pynn, E. Liu, K. W. Herwig, G. S. Smith, J. L. Robertson and W. -R. Chen J. Chem. Phys. **132**, 174509 (2010).
[5] R. Andersson, L. F. Van Heijkamp, I. M. De Schepper and W. G. Bouwman., J. Appl. Cryst. **41**, 868 (2008).
[6] R. Pynn, R. Ashkar, P. Stonaha, A. L. Washington, Physica B **406**, 2350 (2011).
[7] W. C. K. Poon, J. Phys: Condensed Matter **14**, R859 (2002).

THE SHIFTING SHAPES OF FRICTIONAL FLUIDS

LAS FORMAS CAMBIANTES DE LOS FLUIDOS CON FRICCIÓN

B. Sandnes[a †], E. G. Flekkøy[b], K. J. Måløy[b] and J. A. Eriksen[b]

a) Multidisciplinary Nanotechnology Centre, College of Engineering, Swansea University, Singleton Park, Swansea SA2 8PP, UK, b.sandnes@swansea.ac.uk†
b) Department of Physics, University of Oslo, Sem Sælandsvei 24, PO Box 1048 Blindern, 0316 Oslo, Norway
† corresponding author

Remarkable shapes and patterns appear in multiphase flow experiments with frictional fluids. Here we explore the rich dynamics, and map the emerging morphologies in a phase diagram.

Se observan interesantes formas y patrones en experimentos multifásicos sobre fluídos con fricción. Aquí, exploramos esa rica dinámica, y "mapeamos" las morfologías emergentes en un diagrama de fases.

PACS: Pattern formation in granular systems, 45.70.Qj; multiphase flows, 47.55.-t; compaction granular solids, 45.70.Cc; general flow instabilities, 47.20.-k

INTRODUCTION

While displacement patterning in dry granular materials [1,2] and density matched granular suspensions [3-5] have been studied before, the world of settling granular mixtures, where inter-particle friction plays a dominant role, remains largely unexplored. Here we focus on pattern formation in such a frictional fluid, and find a surprising diversity in the morphologies that emerge. Based on our experimental and theoretical results [6-8] we draft a crude phase diagram of the different pattern formation modes we encounter and the phase boundaries between them.

EXPERIMENT

The experiment is simple: Air contained in a syringe is injected into a generic granular-liquid mixture confined in a 500 μm gap between two parallel glass plates of a Hele-Shaw cell (Fig. 1). The syringe pump is driven at a constant compression rate q, and the volume of compressible air in the syringe, V_{air}, adds an adjustable compliance (or stiffness) to the system. The initial filling fraction of granular material –glass beads of 100 μm average diameter– is denoted φ, where we normalize by the close-packing fraction, i.e. $\varphi = 1$ for consolidated grains. The invading air/fluid interface displaces the mixture, and the shifting balance between the contending forces (pressure, frictional, viscous and capillary forces) determines the dynamics as we explore the full range of the chosen experimental variables. In the following we give a somewhat brief description of the most characteristic morphologies that we observe, and refer to a recent paper [8] for more detail regarding experimental setup, results and theoretical considerations.

FRICTIONAL REGIME

Frictional fingers. At low compression rate ($0.01 < q < 0.1$ *ml*/*min*) the invading interface moves slowly and bulldozes up granular material until a layer forms that jams in the gap of the cell. The interface becomes unstable, and fingers of air develop that spawn side-branches as they grow, creating a random labyrinthine structure [6,7]. Fig. 2 (a) shows an example of these frictional fingers, where the dense granular front is seen as a dark band along the interface.

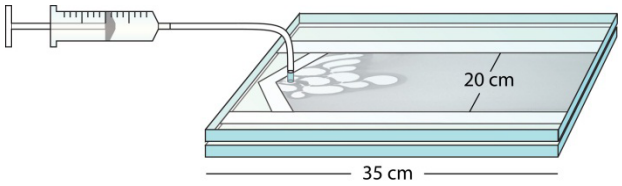

Figure 1: Air is injected into a granular-liquid mixture confined in the gap of a Hele-Shaw cell.

The gas pressure is balanced by the surface tension of the interface and the opposing frictional stress. These forces act locally, and the fingers develop a characteristic width that is independent of system size (unlike viscous fingers). Surface tension acts to widen the curved finger tip, while friction opposes wide fingers since they accumulate thick granular fronts. The characteristic width represents a balance between these two opposing influences. If we increase the amount of granular material in the system, the increased friction shifts the balance, resulting in narrower fingers.